SIGNATURES OF FOREGROUND SKY IN POWER SPECTRA OF REDSHIFTED NEUTRAL HYDROGEN FROM THE EPOCH OF REIONIZATION

Nithyanandan Thyagarajan[1], Daniel C. Jacobs[1], Judd D. Bowman[1]
Draft version May 6, 2014

ABSTRACT

We characterize signatures of foreground radio emission and instrument configuration on the observed power spectra of redshifted Hi 21 cm line emission from the epoch of reionization (EoR) using a baseline (antenna pair) based "delay spectrum" analysis technique. We use the 128-tile Murchison Widefield Array (MWA) instrument configuration for our studies. Our analysis is centered around 185 MHz with 30.72 MHz bandwidth at 40 kHz frequency resolution. We simulate the delay spectrum response of interferometers with antenna pair spacings up to $\sim$ 315 m, for the first time, to an all-sky foreground model consisting of diffuse (on scales $\gtrsim 0°.85$) and compact Galactic and extragalactic emission. By matching simulated parameters to those of a subset of first season of observing with the MWA, we identify and verify key foreground and instrumental signatures seen in data. A wedge-shaped region of foreground contamination in the delay spectra is confirmed. There is a spillover from this contamination into relatively foreground–free regions (*EoR window*) in the delay spectrum caused due to the spectral properties of foreground emission and the instrument. Due to projection effects, diffuse emission produces edge-heavy features. Features in the inner regions of the wedge are predominantly due to compact foreground objects. This results in a "pitchfork" shaped delay spectrum. We provide a practical diagnostic tool for scheduling EoR observations that helps in reducing foreground contamination.

Keywords: large-scale structure of Universe — methods: statistical — radio continuum: galaxies — radio lines: general — reionization — techniques: interferometric

1. INTRODUCTION

After the CMB epoch, the period in the history of the universe often referred to as the *dark ages* was followed by the epoch of reionization (EoR). This was a period of non-linear growth of density perturbations and astrophysical evolution. Studying the epoch of reionization holds the key to understanding this evolution. Recently, oberving the redshifted 21 cm spin transition of neutral hydrogen has emerged as one of the most promising experiments to fill the gaps in our understanding of the universe's history.

Sensitive instruments such as the Square Kilometer Array (SKA) are required for direct observation and tomography of redshifted Hi. Numerous precursors to the SKA such as the Murchison Widefield Array (MWA; Lonsdale et al. 2009; Tingay et al. 2013), the Low Frequency Array (LOFAR; van Haarlem et al. 2013), and the Precision Array for Probing the Epoch of Reionization (PAPER; Parsons et al. 2010) have become operational with enough sensitivity for a statistical detection of the EoR Hi power spectrum.

One of the key challenges in the statistical detection of power spectrum of the redshifted Hi signal arises from the contamination by Galactic and extragalactic foregrounds (see, e.g., Di Matteo et al. 2002; Zaldarriaga et al. 2004; Furlanetto et al. 2006). Morales & Hewitt (2004) show that the inherent isotropy and symmetry of the EoR signal in frequency and spatial wavenumber (k) space make it distinguishable from sources of contamination which lack such symmetry. Foreground removal

techniques rely on the spectral smoothness of foreground emission (Morales et al. 2006; Bowman et al. 2009; Liu & Tegmark 2011; Parsons et al. 2012; Dillon et al. 2013).

Precise understanding of these foreground signatures is necessary in order to remove foreground systematics from the measured power spectrum. Considerable effort has been made in mapping the residual foreground signatures in observed power spectrum (Thyagarajan et al. 2013; Pober et al. 2013; Morales et al. 2012; Trott et al. 2012; Datta et al. 2010; Bowman et al. 2009) after foreground subtraction.

In this paper, in one of the most detailed characterizations to date, using an interferometer (antenna pair) based delay spectrum technique, we demonstrate the signatures of unsubtracted diffuse and compact foreground models in delay spectrum, a quantity closely related to the sought power spectrum. We explore the diversity in these signatures as a function of observation and instrument parameters and confirm our findings with data obtained from the MWA.

We have organized the rest of the paper as follows. §2 defines the delay spectrum and its relation to the power spectrum. §3 and §4 describe the MWA instrumental parameters and observation parameters used in this study respectively. In §5, we describe our data analysis. In §6, we describe the building blocks of our delay spectrum modeling including the foreground models used. Here, we also establish that the results of modeling and data analysis match with each other. In §7, we present a detailed analysis of the signatures of foregrounds on the modeled delay spectrum and its dependence on instrumental and observation parameters. In §8, we use our understanding to grade the delay spectrum as a function

[1] Arizona State University, Tempe, AZ 85287, USA; e-mail: t_nithyanandan@asu.edu

of local sidereal time (LST) in order to obtain a useful diagnostic for planning future observations. In §9, we present our summary and conclusions.

2. DELAY SPECTRUM

Interferometer array data known as *visibilities*, $V_f(\overline{\mathbf{u}}, f)$, are correlations between electric fields measured at different frequencies (f) by different antenna pairs with separation vectors $\overline{\mathbf{x}}$, where $\overline{\mathbf{u}} \equiv \overline{\mathbf{x}} f/c$ and c is the speed of light. $\overline{\mathbf{u}}$ is related to transverse spatial frequency modes ($\overline{\mathbf{k}}_\perp$) of brightness distribution of the sky as $\overline{\mathbf{k}}_\perp \equiv 2\pi\overline{\mathbf{u}}/D(z)$, where $D(z)$ is the transverse comoving distance at a redshift z. If $I(\overline{\mathbf{l}}, f)$ is the emission at different frequencies on the sky as a function of direction unit vector ($\overline{\mathbf{l}}$) specified as direction cosines, $V_f(\overline{\mathbf{u}}, f)$ represents the Fourier decomposition of $I(\overline{\mathbf{l}}, f)$ attenuated by the antenna's angular power pattern $A(\overline{\mathbf{l}}, f)$, into transverse spatial frequency components. Taking into account the instrumental bandpass weights $W_f(f)$, this relation can be written as:

$$V_f(\overline{\mathbf{u}}, f) = \int A(\overline{\mathbf{l}}, f)\, I(\overline{\mathbf{l}}, f)\, W_f(f)\, e^{-i2\pi\overline{\mathbf{u}}\cdot\overline{\mathbf{l}}}\, \mathrm{d}^2\overline{\mathbf{l}}. \quad (1)$$

We define the *delay spectrum* $V_\eta(\overline{\mathbf{u}}, \eta)$ to be the inverse Fourier transform of $V_f(\overline{\mathbf{u}}, f)$ along the frequency coordinate:

$$V_\eta(\overline{\mathbf{u}}, \eta) = \int V_f(\overline{\mathbf{u}}, f)\, W_f'(f)\, e^{i2\pi\eta f}\, \mathrm{d}f, \quad (2)$$

where, $W_f'(f)$ is a frequency window weighting function which can be chosen to control the quality of the delay spectrum (Thyagarajan et al. 2013; Vedantham et al. 2012). η represents the signal delay between the antenna pairs in an interferometer given by:

$$\eta = \frac{\overline{\mathbf{x}} \cdot \overline{\mathbf{l}}}{c} = \frac{\overline{\mathbf{u}} \cdot \overline{\mathbf{l}}}{f}. \quad (3)$$

We use the terms delay and lag interchangeably in the rest of this paper.

Since we are studying a redshifted HI spectral line, f is a measure of cosmological distance along the line of sight. Consequently, η is a measure of line of sight spatial frequency, $k_\parallel$. Thus, $|V_\eta(\overline{\mathbf{u}}, \eta)|^2$ is directly related to the spatial power spectrum of redshifted HI distribution, $|V(\overline{\mathbf{k}}_\perp, k_\parallel)|^2$. However, foreground objects emit in radio frequencies and contaminate the signals from the redshifted HI. Due to their spatial and spectral properties, $V_\eta(\overline{\mathbf{u}}, \eta)$ also contains contamination from foreground radio sources (Thyagarajan et al. 2013; Trott et al. 2012; Morales et al. 2012; Bowman et al. 2009). These contaminations have to be characterized precisely in order to reduce their impact on redshifted HI power spectrum detection sensitivity. We, heareafter, examine in detail the delay spectrum of emission from unsubtracted foreground objects and compare with preliminary observations with the MWA.

3. INSTRUMENT PARAMETERS

We use the 128-tile layout of the MWA (Beardsley et al. 2012). We choose a center frequency of 185 MHz with a bandwidth of 30.72 MHz divided into 768 frequency channels each of width 40 kHz. The choice of

center frequency translates to $z \approx 6.68$ for the 21 cm spin flip transition of HI. The bandwidth was chosen to be close to the maximum instantaneous value of the MWA in order to maximize the resolution in delay coordinates and obtain detailed characteristics of delay spectra from foregrounds. We restrict our analysis to the innermost 2000 pairs covering $|\overline{\mathbf{x}}| \leq x_{\max} \approx 315$ m, or $|\overline{\mathbf{u}}| \leq u_{\max} \approx 157.5$ at a frequency of 185 MHz. These interferometers are responsive to transverse spatial structures on scales $\gtrsim 1/u_{\max} \approx 22'$.

The bandpass weights in the frequency window of the MWA are obtained through a 8-tap Polyphase Filter Bank (PFB) using a Kaiser window with the β parameter set to 5. The bandpass weights consist of coarse frequency channels of width 1.28 MHz each of which contains 32 finer frequency channels of width 40 kHz. Our analysis, therefore, contains 24 coarse channels. As the data are subsequently bandpass calibrated, the bandpass weights are normalized to unity. But in the edges of the coarse channels where the bandpass correction factors are $\gtrsim 3$, this correction makes the edge channels significantly noisy compared to the rest of the spectrum. Thus, we remove 2 fine channels from each side of the coarse channel edges from our data. This constitutes $W_f(f)$ in equation 1. The bandpass properties used in this paper are illustrated in figure 1.
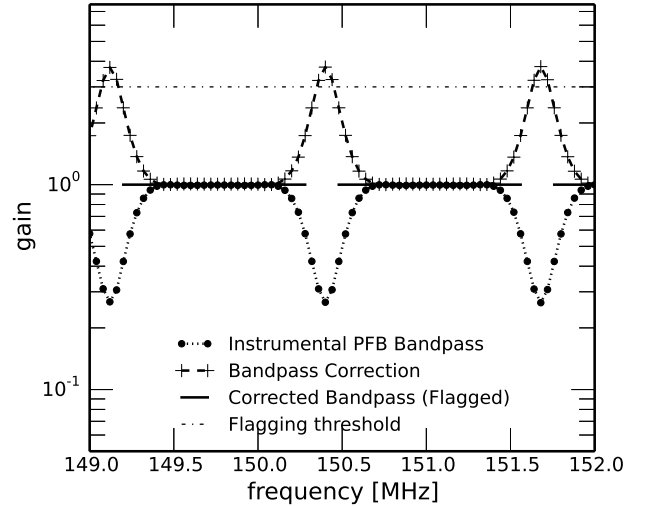
Figure 1. Bandpass properties used in modeling and analysis of delay spectrum of MWA visibilities. The filled circles joined by dotted lines show the 8-tap PFB bandpass shapes obtained using a Kaiser window with parameter $\beta = 5$. The *plus* symbols joined by dashed lines are the bandpass correction factors. The dot-dashed line represents the threshold for bandpass correction factor above which frequency channels are flagged. The solid line shows the flagged and gain–corrected bandpass shape, $W_f(f)$. These properties hold for the entire bandwidth of 30.72 MHz centered around 185 MHz.

Thermal noise in simulated visibilities is estimated assuming a system temperature of $T_{\mathrm{sys}} = 440$ K (Bowman et al. 2006) for all frequency channels for all interferometers throughout the course of observation. We take into account the increase in thermal uncertainty in frequency channels that results due to aforementioned bandpass correction.

The power pattern of a MWA tile, $A(\overline{\mathbf{l}}, f)$ in equation 1,

over the entire hemisphere is modeled based on a 4×4 phased array of half-wave dipoles. Hereafter, we use the terms tile and antenna interchangeably to refer to the MWA tile.

4. OBSERVATION PARAMETERS

One of the primary targets for EoR observations with the MWA is a patch of sky centered around RA = 00h 00m 00.00s, Dec = -30° 00′ 00″.0. This is one of the regions of low foreground emission within 27° from the zenith. The MWA tracks a patch of sky through beams formed and steered electronically by changing delay settings between a phased array of dipoles in a MWA tile. These beamformer delay settings can be changed only in discrete steps. Accordingly, observations were made in a "drift and shift" (D-S) mode. Figure 2 shows the direction of pointing of MWA tiles during the course of the observation. The sky is allowed to drift for a certain period of time (usually ∼ 30 mins) before the discrete shifts in the beamformer delay settings position the beam to be centered again on the patch of sky. This process is repeated throughout the course of the observation ≈ 4.86 hours.
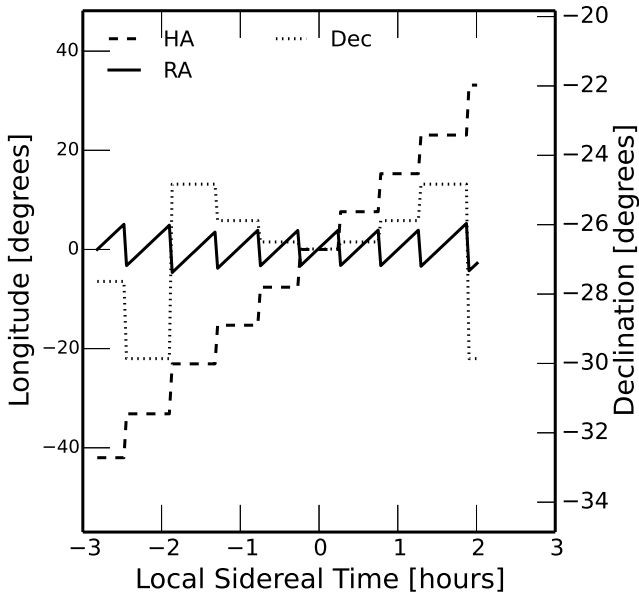
Figure 2. MWA tile pointing directions during the course of the observation. The x-axis refers to the Local Sidereal Time (LST) in hours. The axis on the left refers to longitudes, namely, Right Ascension (RA) and Hour Angle (HA) in degrees. Negative values of RA, HA, and LST are to be interpreted as having been wrapped around by 360° or 24 hours. The axis on the right refers to the declination of the pointing direction. The RA, HA, and declination are plotted with solid, dashed and dotted line styles respectively. A "drift and shift" scheme is used. The sky is allowed to drift for ∼ 30 mins before the beamformer delay settings change in a discrete step to center the beam around RA = 00h 00m 00.00s, Dec = -30° 00′ 00″.0.

5. DATA ANALYSIS

Describe the data analysis here.

Throughout this paper, $\overline{u}$ is assumed to be on a coordinate system aligned with the local east and local north directions at the MWA site. For the conventions

of Fourier transform and its inverse we use in this paper, in accordance with equation 3, signals from the sky towards east and north are recorded with positive delays on eastward and northward baselines respectively. For instance, at the beginning of the observation, the Galactic center is on the far west just about to set. Signals from this direction are recorded with a negative delay on interferometers oriented towards the east. Similarly, signals from directions eastward of the local meridian arrive with positive delays on eastward interferometers. In subsequent discussions, unless mentioned otherwise, all the snapshot visibilities are assumed to be phased to zenith.

For purposes of geometrical intuition, we restrict the orientation (θ_b measured anti-clockwise from East) of all baselines to lie in the range $-67°.5 \leq \theta_b < 112°.5$. Baselines in the other half-plane measure conjugate visibilities with delays of equal magnitude but of opposite sign and hence are ignored in our analysis.

5.1. Deconvolution along Delay Axis

Subsequently, we obtain the delay spectrum of these visibilities using equation 2 while choosing $W'_f(f)$ to be a *Blackman–Nuttall* window function for its superior sidelobe suppression as described in Thyagarajan et al. (2013). Due to periodic gaps in frequency bandpass occurring in intervals of 1.28 MHz (see figure 1), the delay spectrum is expected to contain harmonics of actual foreground emission repeated at intervals of 0.78 μs. Hence, we have employed deconvolution by *CLEAN* algorithm (Taylor et al. 1999) along the delay axis (Parsons & Backer 2009; Parsons et al. 2012) to rid the delay spectra of such artifacts. The convolving kernel for the algorithm is given by the inverse Fourier transform of the instrumental bandpass shape.

5.2. Delay Spectrum from Data

Put up plots here and discuss them.

Despite the deconvolution, we still see leakage beyond the cleaned regions indicating the inability of the deconvolution algorithm to fit the data perfectly. This is predominant at short baselines. This is because the maximum delay envelope (boundary of the wedge) consists of mixed emission from large portions of the sky into a narrow range of delays and the deconvolution algorithm does not have sufficient support in delay space to fit the delay spectrum. However, we note that the purpose of deconvolution is to rid the delay spectra of instrumental artifacts to the best extent possible in order to see the underlying signatures of foreground emission. It is not our intention in this paper to use the deconvolution as a foreground removal tool. Hence, our discussion and conclusions still hold despite imperfections in deconvolution.

6. DELAY SPECTRUM MODELING

Below we describe the foreground model we have used in modeling the measured delay spectra.

6.1. Foreground Model

An instrument such as the MWA has a very wide field of view (∼ 30° at 185 MHz) for imaging purposes. In the context of EoR HI power spectrum it has been shown that unsubtracted forground sources anywhere in the horizon directly contaminate the spatial frequency

modes in the power spectrum. In addition, this contam-
ination also spills over into the relatively cleaner regions,
called *EoR window*, due to spectral properties of the in-
strument and the foregrounds (Thyagarajan et al. 2013;
Pober et al. 2013; Vedantham et al. 2012; Parsons et al.
2012). Thus, it is important to consider an all-sky model
for foreground objects in evaluating the features seen in
the power spectrum.

Beardsley et al. (2013) estimated the sensitivity of the
MWA to EoR H I power spectrum detection taking into
account thermal noise effects in the *Eor window*. Thya-
garajan et al. (2013) estimated the sensitivity taking
into account the spillover from foreground contamination
from unsubtracted extragalactic point sources in the $\widehat{EoR}$
window besides thermal noise. In this paper, we include
the diffuse Galactic emission for a comprehensive under-
standing of foreground signatures in the power spectrum.
We use an all-sky foreground emission model that con-
sists of diffuse and bright compact components.

6.1.1. *Diffuse Foreground Model*

For the diffuse component, we use an all-sky radio
foreground model from de Oliveira-Costa et al. (2008)
to estimate the emission at 185 MHz. Since this map
is predominantly based on the 408 MHz all-sky map of
Haslam et al. (1982) which has an angular resolution of
$0°.85$, we smoothed the 185 MHz diffuse emission map
to the same resolution. However, to avoid any artifacts
from sampling this map, we sample it at $\approx 27'$ intervals.
Using the same source model, we also obtain the diffuse
emission maps at 140 MHz and 160 MHz to estimate the
spectral index map of the diffuse emission model.

6.1.2. *Compact Foreground Model*

We use a combination of NRAO VLA Sky Survey
(NVSS; Condon et al. 1998) at 1.4 GHz and Sydney Uni-
versity Molonglo Sky Survey (SUMSS; Bock et al. 1999;
Mauch et al. 2003) at 843 MHz due to their similar flux
sensitivity and angular resolution, and complimentary
survey footprints covering the entire sky. The SUMSS
catalog covers the sky with declination $\delta < -30°$ with a
limiting peak brightness of 6–10 mJy/beam and an an-
gular resolution of $\sim 45''$. The NVSS covers the sky with
$\delta > -40°$ with a similar angular resolution and a limiting
flux density of ≈ 2.5 mJy for discrete sources.

From the SUMSS catalog, we select compact sources
whose deconvolved major axes are equal to 0. From the
NVSS catalog, we excluded objects that overlap with
those in the SUMSS survey footprint. Compact sources
from NVSS were selected if the convolved major axes
were not greater than $\approx 47''$, which is almost equal to the
angular resolution of the survey. Using a mean spectral
index of $\langle \alpha \rangle = -0.83$ (flux density, $S(f) \propto f^\alpha$) obtained
by Mauch et al. (2003) for both NVSS and SUMSS cata-
log objcts, we calculate the corresponding flux densities
at 185 MHz, S_{185}. From this subset, we choose compact
objects with $S_{185} \geq 10$ Jy. We verified that our selection
criteria ensure a similar areal density of sources in the
two surveys.

Based on these criteria, we selected 133 sources from
the SUMSS catalog and 336 sources from the NVSS cat-
alog. The selection of such bright compact objects is
not affected by minor differences in sensitivity of the two

surveys. Together with the diffuse foreground model, we
obtain an all-sky foreground model consisting of both
compact and diffuse emission.

6.2. *Comparison with Data*

With the aforementioned all-sky foreground model,
and instrumental and observational parameters, we sim-
ulate visibilities using equation 1. We consider two snap-
shots, one at the beginning and one during the middle of
the observation, to explain the signatures of foregrounds
seen in the modeled and observed data. The first snap-
shot is pointed at RA = $4°.387$, Dec = $-29°.86$ at 22.08
hours LST while the second is pointed at RA = $+1°.320$,
Dec = $-26°.70$ at 0.09 hours LST. In both cases the visibil-
ities are phased to zenith corresponding to RA = $-28°.8$,
Dec = $-26°.701$, and RA = $1°.35$, Dec = $-26°.701$ respec-
tively. Signals from the phase center are received simu-
latneously with no delay between the interferometers.

Figure 3 shows the amplitude of delay spectrum from
two snapshots, one each at the beginning, and middle of
the observation. Notice the close resemblance in ampli-
tude and structure with those obtained from data.
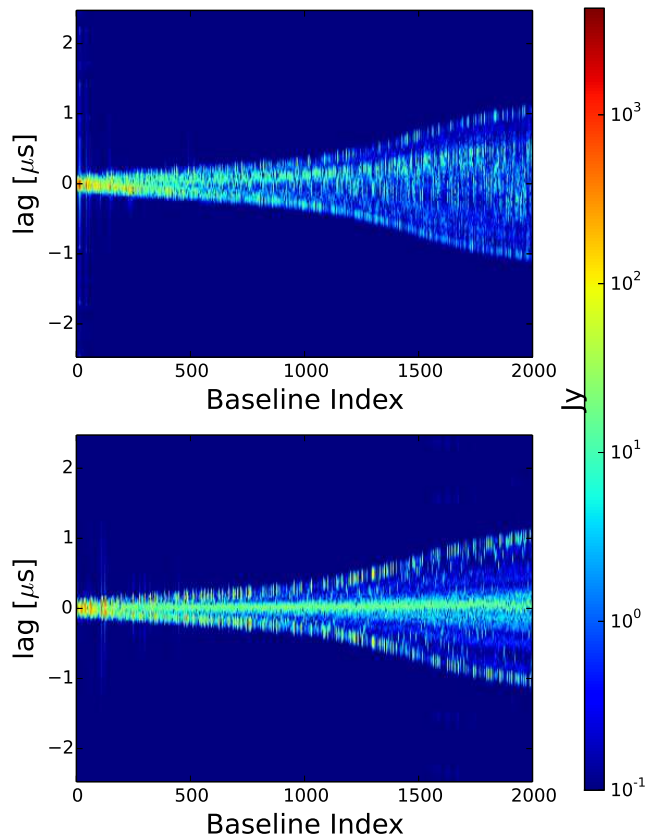
Figure 3. Delay spectrum for the all-sky foreground model at
two pointing positions. *Top:* At the beginning of the observation.
Bottom: At the middle of the observation.

We examined the delay spectra obtained from data and
through modeling in more detail by comparing the two
on a few selected baselines. They are found to match
well with each other.

7. DELAY SPECTRUM ANALYSIS

Having established that results from modeling match those from data, we proceed to examine in further detail the signatures seen in the modeled delay spectra.

A number of factors are responsible for the characteristics noted in the delay spectra obtained from data and through modeling. We address these factors below:

- *Sky Model*: Our model of the sky consists of bright compact sources and diffuse emission. Both of these kinds of emission are anisotropic and so is the resulting composite model. In fact, the pointing for MWA observations is chosen from regions of low foreground emission. In our study, we have divided the transiting sky into four different "bowtie" shaped regions with equal areas and zenith as the origin. This results in the ability to attribute the features in the delay spectrum to eight different sectors of the sky.

- *LST*: The LST is also a crucial factor in determining the scheduling of the observation. The LST of our data ranges from $\sim$ 21 hours through $\sim$ 2 hours (see figure 2). For comparisons, we choose two snapshot observations at 22.09 hours and 0.08 hours LST.

- *Baseline Orientation*: Since the spatial structure of our foreground model is not expected to be isotropic, we divide our interferometer baselines by their orientation ($\theta_{\rm b}$) measured counter-clockwise from East. We use the following bins: $-67\overset{\circ}{.}5 \leq \theta_{\rm b} < -22\overset{\circ}{.}5$, $-22\overset{\circ}{.}5 \leq \theta_{\rm b} < 22\overset{\circ}{.}5$, $22\overset{\circ}{.}5 \leq \theta_{\rm b} < 67\overset{\circ}{.}5$, and $67\overset{\circ}{.}5 \leq \theta_{\rm b} < 112\overset{\circ}{.}5$. The bin centers are oriented towards South-East, East, North-East, and North respectively.

- *Tile Pointing and Power Pattern*: Since the MWA tiles are phased electronically, the power pattern of the tile changes in any observing mode that tracks the source. Our observations consist of a combination of allowing the sky to drift and tracking the sky. In our study, we take into account the effect of changing power pattern of the antennas on the delay spectrum. For convenience, we refer to the first and second pointing used at the chosen LST as off-zenith and on-zenith pointings respectively.

- *Instrumental Bandpass*: The instrumental bandpass characteristics have a direct effect on the delay transform owing to a Fourier relationship between the two. Due to excision of noisy edge channels repeated in each coarse channel of our bandpass, we see repeated patterns of the *foreground wedge* in the delay spectra. As already mentioned earlier, we have used the deconvolution algorithm (*CLEAN*) to rid the delay spectra of band shape effects. Since this paper focuses on studying the effects of foreground on the delay spectra, we do not pursue the characterization of artifacts from the band shape and imperfections in *CLEAN* deconvolution.

The signatures we henceforth identify in the delay spectrum are characterized as arising out of the aforementioned factors. Due to numerous combinations of such factors, we use unique codes for these combinations as described in table 1. The first column refers to the place holder of the specific parameter in the code sequence from left to right. The parameter codes are specified in this order. The second column gives the parameter used in describing features in delay spectrum. The third column denotes the code describing the parameter. Snapshot index uniquely specifies the snapshot and carries a numeric code (1 and 2 for off-zenith and on-zenith snapshots respectively) leading the code sequence. Following this, the type of emission is specified as compact, diffuse, Galactic center, or Galactic plane using codes C, D, GC, or GP respectively. Although in reality, a feature could be due to a combination of emission types, the code we use refers to the predominant type of emission that can be attributed to the feature. The next code specifies the direction of this predominant source of emission. The code values for the direction of emission are the usual abbreviations of the cardinal and ordinal directions besides Z (zenith). Following this is the code for the baseline orientation bin in the half-plane specified as S, SE, E, and NE along directions south, south-east, east, and north-east respectively. Code 'A' is used to refer to all baselines. Finally, the parameter describing the region of antenna power pattern coincident with the predominant emission responsible for the feature is specified as P (primary lobe) and S (secondary lobe). The secondary lobe code carries a numeral suffix to further specify uniquely the sidelobe in the direction of emission. For example, a feature code 1-D-W-E-P indicates it is from the first snapshot (1) arising due to diffuse emission (D) westward (W) of zenith observed by predominantly eastward (E) baselines centered on the primary beam (P) of the antenna power pattern. Similarly, feature code 2-GC-W-NE-S3 implies the feature is seen in the second snapshot (2) due to the Galactic Center (GC) that is westward (W) of zenith by north-eastward (NE) baselines and the region coincides with the third sidelobe (S3) in the direction of emission.

We wish to note that numerous features overlap at varying levels of significance as a result of various combiantions of parameters. We assign the features to their predominant causes. Secondly, we have used noiseless cases to clearly illustrate the observed foreground signatures. With the addition of noise in the visibilities which is subject to observing time, some of the weaker features may not be as prominently visible.

7.1. *Diffuse Foregrounds*

Figure 4 shows the noiseless delay spectra due to diffuse emission. Figure 4a and 4b correspond to off-zenith and on-zenith snapshots respectively. In general, shorter baselines are expected to be receptive to large scales such as from diffuse emission as well as from small scales from compact objects. This effect is most clearly visible in the on-zenith snapshot noted by feature code 2-D-Z-A-P which stands for the signature observed due to diffuse emission from zenith direction on short baselines of all orientations restricted primarily to the primary beam. This is a notable feature on baselines of length $\lesssim 60$ m. For a frequency of 185 MHz, this length scale corresponds to angular scales of $\gtrsim 1\overset{\circ}{.}5$ on the sky. This feature is noted only for diffuse emission from inside the primary beam.

The most prominent feature, however, is 1-GC-W-E-

Table 1
Codes used to describe signatures in delay spectrum.

Order	Parameter Description	Code
1	Snapshot index	1, 2, ...
2	Type of emission	C (compact), D (diffuse), GC (Galactic center), GP (Galactic plane)
3	Direction of emission	E (east), N (north), W (west), S (south), Z (zenith)
		NE (north-east), NW (north-west), SW (south-west), SE (south-east)
4	Baseline orientation	E (east), S (south), SE (south-east), NE (north-east), A (all)
5	Region in antenna power pattern	P (primary beam), Sn (n-th sidelobe, $n = 1, 2, \ldots$)
	(in the direction of emission)	

S3 in figure 4a. This is noted in the off-zenith snapshot caused by the bright Galactic center which is on the west at an altitude of $\sim 33°$ with ~ 100 minutes remaining before it sets. This emission is observed as it is coincident with the third sidelobe of the power pattern in the westward direction with a neagtive delay of value almost close to the horizon limit on eastward baselines.

7.1.1. *Diffuse Emission On Long Baselines*

Interestingly, in contrast to feature code 2-D-Z-A-P, all the other features in figures 4a and 4b extend from the shortest (~ 7.7 m) to longest baselines (~ 314.7 m). We argue this is because even longer baselines are shortened when projected against directions along the baseline vector towards the horizon while considering an all-sky foreground model. Such a shortening due to projection effects allows diffuse emission from close to the horizon to be observed at maximum delays that correspond to the horizon limit even on long baselines. Feature 1-GP-NE-NE-S2 in figure 4a, and features 2-GP-N-N-S2 and 2-GP-S-N-S2 in figure 4a demonstrate this effect of shortening of baselines. 1-GP-NE-NE-S2 corresponds to emission observed from the Galactic plane from north-eastward directions by north-eastward baselines from the second sidelobe in their power pattern. Features 2-GP-N-N-S2 and 2-GP-S-N-S2 are also Galactic plane emission from southward and northward directions observed by second sidelobes of northward baselines with opposite delays. Owing to their apparent structure in delay spectra, we hereafter refer broadly to this edge-heavy structure as the "two-pronged fork" feature.

Thus, the most notable features from diffuse emission are those from primary beam area on short baselines, bright Galactic center from the third sidelobe, and the two-pronged fork.

7.2. *Compact Foregrounds*

Figure 5 shows the noiseless delay spectra obtained from compact foreground objects. The off-zenith and on-zenith snapshot delay spectra are shown in figures 5a and 5b respectively.

In the off-zenith snapshot, the most prominent feature 1-C-E-E-P arises due to eastward baselines observing the eastward sky at positive delays centered on the primary beam. The next prominent feature 1-C-E-N-P at zero delays arises due to the compact emission from eastward sky centered on the primary beam observed by northward baselines. Features 1-C-NE-NE-S2 and 1-C-W-E-S3 at positive and negative horizon limits are caused by north-eastward sky emission observed by the second sidelobe of north-eastward baselines and westward sky centered on the third sidelobe of eastward baselines respectively.

The most prominent feature in the on-zenith snapshot is 2-C-Z-A-P appearing at zero delays caused by compact sources at zenith observed by all baselines along their primary beams. First and second sidelobes along north and south observed by northward baselines contribute to symmetric positive and negative delays as demonstrated by features 2-C-S-N-S1, 2-C-N-N-S1, 2-C-S-N-S2, and 2-C-N-N-S2.

While compact foreground objects give rise to features throughout the foreground wedge, the primary distinction between delay spectra of compact and diffuse foregrounds is that the latter are predominantly center-heavy when compared to edge-heavy features of the former.

7.3. *All-Sky Composite Foreground Model*

Delay spectra from the all-sky foreground model in our study display a composite feature set drawn from the features of compact and diffuse foreground models. Figures 6a and 6b show the delay spectra for the composite all-sky foreground model. While features from both its constituents occupy and overlap in different regions of the foreground wedge, their relatives magnitudes determine the resultant signatures seen in the delay spectra. For instance, the fork-shaped features of diffuse emission are brighter by a factor $\gtrsim 10$ relative to the compact foreground features at the edges of delay spectra in the respective snapshots. Hence, features 1-C-W-E-S3 and 1-C-NE-NE-S2 in figure 5a have been masked by features 1-GC-W-E-S3 and 1-GP-NE-NE-S2 repecively from diffuse emission in figure 4a. Similarly, the edge features 2-C-S-N-S2 and 2-C-N-N-S2 from compact objects in figure 5b have been masked by diffuse emission features 2-GP-S-N-S2 and 2-GP-N-N-S2 respectively in figure 4b.

On the other hand, in central and inner regions of the wedge, clearly the center-heavy compact foreground model features dominate by $\gtrsim 2$ orders of magnitude relative to features arising out of diffuse emission. This is quite evident since almost all the diffuse emission features are confined to the edges of the wedge. Further, 2-D-Z-A-P in figure 4b is completely masked by 2-C-Z-A-P in figure 5b. Thus the inner regions of the wedge consist only of compact foreground features 1-C-E-N-P and 1-C-E-E-P in figure 6a and 2-C-Z-A-P, 2-C-S-N-S1 and 2-C-N-N-S1 in figure 6b.

Figures 6c and 6d show the delay spectra from the diffuse and compact foreground models as well as from the composite model for the off-zenith and on-zenith snapshots respectively for a selected baseline labeled as "155-154". This baseline is of length $\simeq 201$ m and orientation $\theta_b \simeq 13°.7$. These are effectively vertical slices of figures 6a and 6b through the baseline location. The horizon delay limits are shown by vertical gray lines. Diffuse emission is negligible in the off-zenith snapshot except at the negative horizon delay limit. This is identified to be feature 1-GC-W-E-S3 noted in figure 6a due to the bright
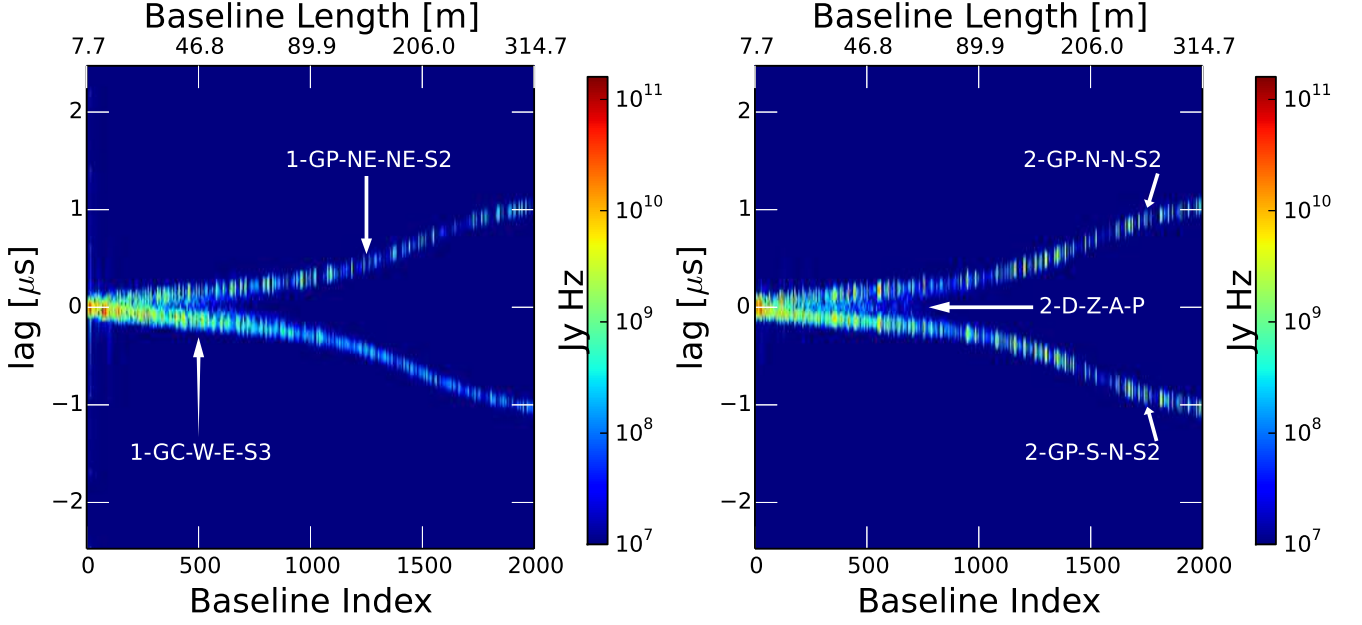
(a) Off-zenith delay spectra from diffuse foreground model   (b) On-zenith delay spectra from diffuse foreground model

Figure 4. Delay spectrum visibility amplitudes (in units of Jy Hz) from diffuse foreground emission obtained on baselines of length ≲ 314.7 m. The left and right panels correspond to off-zenith and on-zenith snapshots respectively. These are noiseless delay spectra obtained after *CLEAN* deconvolution along delay axis. A logarithmic color scale is used. Most prominent features are due to the bright Galactic center shining through the third sidelobe (1-GC-W-E-S3), diffuse emission of short baselines at zero delays (2-D-Z-A-P), and diffuse emission on long baselines close to the horizon limit leaking in through the second sidelobes (1-GP-NE-NE-S2, 2-GP-N-N-S2, and 2-GP-S-N-S2). Features from diffuse emission are predominantly edge-heavy resembling a two-pronged fork. See text for a detailed description of these features.
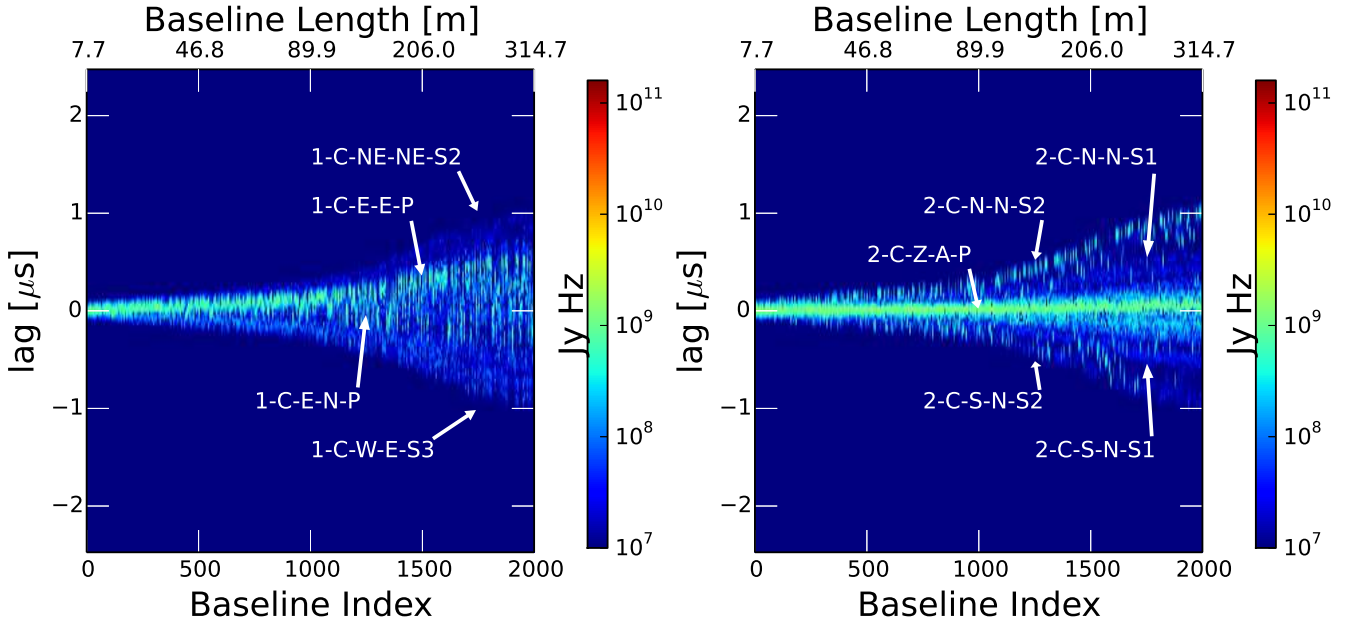
(a) Off-zenith delay spectra from compact foreground objects   (b) On-zenith delay spectra from compact foreground objects

Figure 5. Same as figure 4 but for compact foreground objects. Color scale is the same as in figure 4. The different features annotated are a result of emission observed by compact foreground objects through primary beam and sidelobes. Broadly, signatures in delay spectra of compact foreground objects are center-heavy in appearance. See text for a detailed description of the different features.

Galactic center on the westward sky observed by eastward baseline through its third sidelobe. All the other features are predominantly due to compact foreground objects. The peak at delay of $\sim 0.3\,\mu$s is identified as feature 1-C-E-E-P in figure 6a. The peak at zero delay is from feature 1-C-Z-A-S1 while the other secondary peaks arise compact sources coincident with sidelobes of the power pattern. In the on-zenith snapshot, the feature 1-C-E-E-P has transformed to feature 2-C-Z-A-P due to change in pointing position. The diffuse emission is confined to the edges labeled by features 2-D-W-E-S2 and 2-D-E-E-S2. All intermediate peaks are due to compact foreground objects observed through the different sidelobes of the antenna power pattern.

Thus the composite all-sky foreground model results in a delay spectrum structure that captures both the edge-heavy two-pronged fork structure from diffuse foreground emission and the center-heavy features from compact foreground objects. Hereafter, we refer to this structure as a "three-pronged pitchfork".

8. FOREGROUND GRADING DIAGNOSTIC FOR OBSERVATIONS
9. SUMMARY

Our primary motivation in this work is to analyze the signatures of foreground components in the measured delay spectrum. Such an analysis will be helpful in extending our knowledge on the challenge posed by foregrounds in studying the EoR and in devising techniques to mitigate EoR signal contamination from foregrounds. This is one of the first studies that uses an all-sky foreground model to study the resultant signatures on EoR delay spectrum.

Using parameters that match the instrument and EoR observations using the MWA, and an all-sky foreground model that consists of diffuse emission on scales $\gtrsim 0\overset{\circ}{.}85$ and bright compact sources from the NVSS and SUMSS catalogs, we model delay spectra obtained with the MWA on each of its baselines of length $\lesssim 315$ m. We confirm that the modeled delay spectra match the data obtained with the MWA. A wedge shaped structure is clearly noted as predicted by previous studies.

We use our simulations in a noiseless scenario to understand many of the foreground signatures seen in the delay spectra. We find that the delay spectra depend on observing parameters such as antenna pointing and LST, instrument parameters such as antenna power pattern and bandpass shape, and foreground parameters such as the nature of emission, spectral index, etc. A *CLEAN* deconvolution in delay-space was applied to remove the contaminating harmonic effects of frequency flagging.

Notable features caused by diffuse emission include the bright Galactic center at the edge of the horizon to be observed through the far sidelobe of the antenna power pattern. As expected, diffuse emission in the primary beam of the antenna power pattern is present on short baselines of length $\lesssim 60$ m. Quite surprisingly, diffuse emission also leaves its footprint on long baselines on either side of the delay axis at the horizon delay limits. This clearly indicates that long baselines appear to

be shortened in the direction of the horizon along the baseline vector and these short projected baselines are responsive to large scale diffuse emission. Thus, one of the most important findings of this study is the response of even long baselines to diffuse structures. The characteristic signature of diffuse emission appears to be a roughly symmetric edge-heavy feature taking the form of a *two-pronged fork*.

On the other hand, compact foreground objects predominantly map onto inner regions of the wedge. Features arising from compact sources coincident with primary beam and sidelobes of antenna power pattern are clearly noted. In general, compact objects produce delay spectrum signatures that are center-heavy, in stark contrast to those from diffuse foregrounds.

A composite all-sky foreground model consisting of diffuse and compact foregrounds gives rise to a combination of edge-heavy fork shaped features from diffuse foregrounds and center-heavy features from compact foreground objects in the delay spectrum. The compact foreground features are brighter by $\gtrsim 3$ orders of magnitude brighter than the diffuse foreground features in the central regions of delay spectrum. On the other hand, the edge-heavy diffuse foreground features in the delay spectrum are $\gtrsim 1$ order of magnitude brighter than that due to compact foregrounds at the edges of delay spectrum. This gives the appearance of a *pitchfork* shape to the resultant delay spectrum.
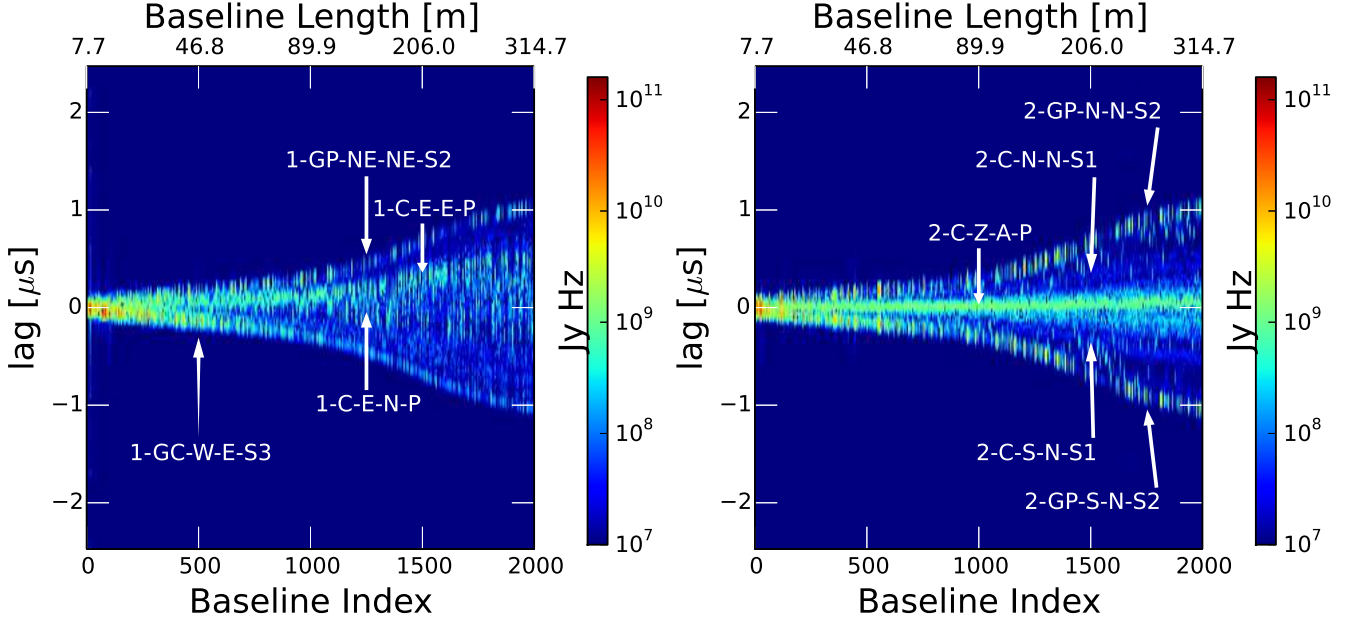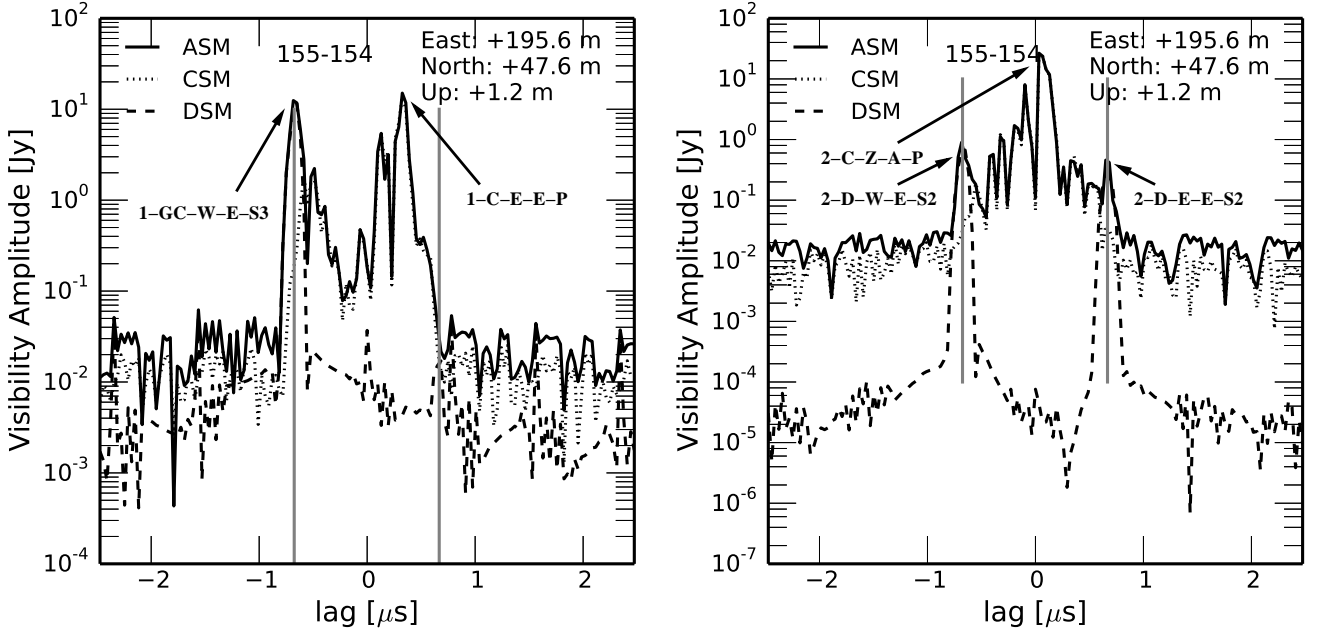
APPENDIX

REFERENCES

Beardsley, A. P., Hazelton, B. J., Morales, M. F., et al. 2012, MNRAS, 425, 1781

(a) Off-zenith delay spectra from composite foreground model

(b) Off-zenith delay spectra from composite foreground model

(c) Off-zenith composite delay spectrum on eastward baseline

(d) On-zenith composite delay spectrum on eastward baseline

Figure 6. *Top*: Same as figure 4 but for a composite all-sky foreground model consisting of both diffuse emission and compact objects. The color scale used is the same. The different features annotated arise from those in figures 4 and 5. Inner regions of the wedge are dominated by center-heavy features such as 1-C-E-N-P, 1-C-E-E-P, 2-C-Z-A-P, 2-C-N-N-S1 and 2-C-S-N-S1 characteristic of compact objects. Outer regions are dominated by edge-heavy fork-shaped features such as 1-GC-W-E-S3, 1-GP-NE-NE-S2, 2-GP-S-N-S2 and 2-GP-N-N-S2 characteristic of diffuse emission. The resultant structure in delay spectrum takes the form of a *pitchfork*. *Bottom*: Slices of delay spectrum visibility amplitudes from the top panel at the location of a selected eastward baseline. The baseline vector is ~ 201 m in length oriented $\sim 13°.7$ measured anti-clockwise from east. The foreground components are: diffuse sky model (DSM, dashed lines), sky made of compact sources (CSM, dotted lines) and all-sky composite model (ASM, solid lines). The gray vertical lines signify the wedge boundaries set by the horizon delay limit. Compact sources dominate the delay spectra in the inner part of the wedge as marked by features 1-C-E-E-P and 2-C-Z-A-P. Edge-heavy fork-shaped features such as 1-GC-W-E-S3, 2-D-W-E-S2 and 2-D-E-E-S2 from diffuse emission are more significant at the edges of the wedge. These give rise to a "pitchfork" appearance. Other secondary peaks inside the wedge are due to compact objects observed through sidelobes of the antenna power pattern. The secondary bumps outside the wedge in all the model components is a result of imperfect deconvolution along delay axis. Refer to text for detailed description of these features.

—. 2013, MNRAS, 429, L5

Bock, D. C.-J., Large, M. I., & Sadler, E. M. 1999, AJ, 117, 1578

Bowman, J. D., Morales, M. F., & Hewitt, J. N. 2006, ApJ, 638, 20

—. 2009, ApJ, 695, 183

Condon, J. J., Cotton, W. D., Greisen, E. W., et al. 1998, AJ, 115, 1693

Datta, A., Bowman, J. D., & Carilli, C. L. 2010, ApJ, 724, 526

de Oliveira-Costa, A., Tegmark, M., Gaensler, B. M., et al. 2008, MNRAS, 388, 247

Di Matteo, T., Perna, R., Abel, T., & Rees, M. J. 2002, ApJ, 564, 576

Dillon, J. S., Liu, A., & Tegmark, M. 2013, Phys. Rev. D, 87, 043005

Furlanetto, S. R., Oh, S. P., & Briggs, F. H. 2006, Phys. Rep., 433, 181

Haslam, C. G. T., Salter, C. J., Stoffel, H., & Wilson, W. E. 1982, A&AS, 47, 1

Liu, A., & Tegmark, M. 2011, Phys. Rev. D, 83, 103006

Lonsdale, C. J., Cappallo, R. J., Morales, M. F., et al. 2009, IEEE Proceedings, 97, 1497

Mauch, T., Murphy, T., Buttery, H. J., et al. 2003, MNRAS, 342, 1117

Morales, M. F., Bowman, J. D., & Hewitt, J. N. 2006, ApJ, 648, 767

Morales, M. F., Hazelton, B., Sullivan, I., & Beardsley, A. 2012, ApJ, 752, 137

Morales, M. F., & Hewitt, J. 2004, ApJ, 615, 7

Parsons, A. R., & Backer, D. C. 2009, AJ, 138, 219

Parsons, A. R., Pober, J. C., Aguirre, J. E., et al. 2012, ApJ, 756, 165

Parsons, A. R., Backer, D. C., Foster, G. S., et al. 2010, AJ, 139, 1468

Pober, J. C., Parsons, A. R., Aguirre, J. E., et al. 2013, ApJ, 768, L36

Taylor, G. B., Carilli, C. L., & Perley, R. A., eds. 1999, Astronomical Society of the Pacific Conference Series, Vol. 180, Synthesis Imaging in Radio Astronomy II

Thyagarajan, N., Udaya Shankar, N., Subrahmanyan, R., et al. 2013, ApJ, 776, 6

Tingay, S. J., Goeke, R., Bowman, J. D., et al. 2013, PASA, 30, 7

Trott, C. M., Wayth, R. B., & Tingay, S. J. 2012, ApJ, 757, 101

van Haarlem, M. P., Wise, M. W., Gunst, A. W., et al. 2013, A&A, 556, A2

Vedantham, H., Udaya Shankar, N., & Subrahmanyan, R. 2012, ApJ, 745, 176

Zaldarriaga, M., Furlanetto, S. R., & Hernquist, L. 2004, ApJ, 608, 622